RSC Advances

ROYAL SOCIETY
OF CHEMISTRY

www.rsc.org/advances

Enhanced photocatalytic activity exhibited by PTh/[Fe(CN)$_3$(NO)(bpy)] 4H$_2$O

nanocomposite fibers via a synergistic approach

Mohd. Hanief Najar[*], Kowsar Majid[*]

Department of Chemistry, National Institute of Technology, Srinagar (J&K) 190 006, India.

Abstract: Successful synthesis of photoadduct, [Fe(CN)$_3$(NO)(bpy)]4H$_2$O and its use as filler in polythiophene (PTh) matrix for synthesizing PTh/[Fe(CN)$_3$(NO)(bpy)]4H$_2$O nanocomposite fibers by chemical polymerization. [Fe(CN)$_3$(NO)(bpy)]4H$_2$O exhibited wide transparency in the entire visible region, thereby showing non-linear optical behavior (NLO) which has been confirmed by second harmonic generation (SHG) test. Fibrous structure of nanocomposite have been confirmed from TEM. Thermal analysis revealed increased thermal stability of nanocomposite fibers than pure PTh. Dielectric study showed a capacitive effect of nanocomposite fibers at low frequencies and a conductivity effect at high frequencies. This behavior may provide absorptive and reflective mechanism to EMI shielding. Meanwhile, higher photocatalytic activity of the present material for methyl orange (MO) dye have been observed than many other two component systems as reported in literature. This has been attributed to the presence of synergistic effect between PTh and photoadduct particles which is believed to play an essential role in affecting the photoreactivity. From BET, surface area of nanocomposite has been found to be 18.9 m^2/g. Main contributing factor to the enhanced photocatalytic activity of nanocomposite fibers has been attributed to the interface contact between PTh and photoadduct particles, as is evidenced by PL measurements. Also, the degradation mechanism of the photocatalytic process has been proposed and the active species involved to cause degradation are confirmed by using different scavengers. Kinetic study

revealed degradation process to follow second order kinetics with an observed rate constant of $7 \times 10^{-4} \, Lmol^{-1}s^{-1}$.

Key Words: photoadduct, polythiophene, nanocomposite, dielectric study, photocatalysis, UV-Visible light

1. Introduction

Dye effluents from textile industries are becoming a serious environmental problem because of their unacceptable color, high chemical oxygen demand and resistance to chemical, photochemical and biological degradation [1]. In this manner, metal oxide nanoparticles such as ZnO, TiO_2 etc. has been widely used to degrade non-biodegradable dyes by photochemical routes [2]. But the major shortcoming of TiO_2 nanoparticles include the low quantum efficiency and the confined utilization of sunlight. In addition to this, many inorganic photocatalysts containing some rear earths have been explored. However owing to their high cost, self-decomposition of photocatalytic reactions, low quantum efficiency, critical drawback of photo-corrosion etc. impair their applications to a great extent [3]. For effective photocatalytic degradation of dyes, the material must be porous, should possess large surface to volume ratio, high charge carrier mobility and slower recombination rate of charge carriers. Such factors are complementary to one another since there are systems having lower surface area are efficient photocatalysts and vice versa [4]. Large surface area leads to efficient adsorption of dye degradation, greater interface contact between different components and easy migration of charge carriers leads to decreased electron-hole pair recombination thereby prolonged the life time of charge carriers. Interface contact is not either enough to increase photocatalytic activity if there is no charge separation, which can occur only once the system

is conducting. This has been reported for graphene based photocatalysts [5, 6]. Keeping this thing into consideration, conducting polymers have attracted much attention especially polythiophene (PTh) owing to its high conductivity, environmentally stable, lost cost, easy synthetic procedure etc. [7]. From literature, enhanced photocatalytic activity of polyaniline-ZnO nanocomposite have been observed for the degradation of dyes like methylene blue and malachite green [8]. Also polyaniline modified TiO_2 composite have been found to exhibit efficient photocatalytic degradation of methyl orange dye [9].

Since transition metal complexes are known to show catalytic properties and many of them especially bypyridyl complexes are good at harnessing light energy and are attractive for solar energy conversion and storage due to their spectral properties, long lifetimes of their excited states and the ease with which they undergo oxidation and reduction reactions. Thus they can be good candidates for photocatalytic activity provided they are coupled with conducting polymers via nanocomposite formation to make them suitable heterogeneous catalysis. Moreover conducting polymers have the advantage of having low ionization energy and high electron affinity due to which their band gap can easily be tuned for better photocatalytic activity. In this direction, the present paper involves the use of a bypyridyl complex of Fe as filler in polythiophene matrix for thermal, dielectric and photocatalytic activities.

2. Experimental

2.1. Materials and Physical measurements

Thiophene (Himedia, India) was distilled and stored at $-5^{\circ}C$ prior to use. Sodium pentacyanonitrosylferrate(II) dihydrate (SNP, Himedia India), anhydrous Ferric Chloride (Fisher Scientific, India), Chloroform (Fisher Scientific, India) were all of analytical reagent

grade. All solutions were prepared in triply distilled water. UV-visible spectra were taken on T80 double beam spectrophotometer (India). Irradiation was done with Osram UV-Visible photo lamp. FTIR spectra was recorded on Perkin Elmer RX-1 FTIR spectrophotometer (USA) using KBr pellets. Surface morphology of the samples was studied on Hitachi SEM model S-3600N (Japan). XRD was conducted using a Rigaku D/max-2500 X-ray diffractometer with Cu Kα1 radiation ($\lambda = 1.5406A°$) (Japan). Thermal analysis of the samples was done using SDT Q600 V8.3 Build 101 instrument (Germany) in N_2 atmosphere at a heating rate of $10°C$ min^{-1}. The temperature range was from ambient to $700°C$. An aluminum pan was used as a reference. Dielectric studies have been carried out using 150MHz Precision Impedance analyzer, Wayne Kerr 6520A. Photocatalytic activity was carried out for 50 ppm of 100 ml methyl orange (MO) dye solution containing 0.5 g of photocatalyst (nanocomposite), was irradiated using Xenon arc lamp. PL measurements have been carried out by F-2700 FL Spectrophotometer. BET analysis has been carried out by Smart Sorb 92/93 Surface area analyzer.

Photocatalytic activity of the nanocomposite was measured against methyl orange (MO) dye under UV-Visible light irradiation using 470 W Xe-arc lamp. In the photocatalytic photo-degradation experiment, 100 ml of dye solution (50 ppm) was magnetically stirred with 0.5g of photocatalyst (nanocomposite fibers) for 45 minutes in the dark to ensure the establishment of adsorption/desorption equilibrium. This has been confirmed from constancy of percent adsorption of MO dye in dark. During irradiation, 5ml aliquots after every 10 minutes were samples and then analyzed by T80+ double beam UV-Visible spectrophotometer for concentration determination using Bear Lambert Law ($\lambda_{max} = 485$ nm and $\varepsilon = 24600$). The photo-degradation of MO dye via the photocatalytic activity of nanocomposite as photocatalyst was calculated using the formula:

$$\text{Photo-degradation of MO dye (\%)} = (C_o - C_t)/C_o \text{ x } 100$$

Where C_o is the initial MO dye concentration before irradiation and C_t is the concentration of MO dye at different irradiation times [10].

2.2. Synthesis of photoadduct: $[Fe(CN)_3(NO)(bpy)] \cdot 4H_2O$

Photoadduct is a photoproduct obtained by the photosubstitution of ligands in a transition metal complex with some desired ligands of choice. The synthesis of photoadduct, $[Fe(CN)_3(NO)(bpy)] \cdot 4H_2O$ has been carried out according to following procedure: an equimolar mixture of sodium pentacyanonitroxylferrate(II) dihydrate (SNP) and 2,2-bypyridyl in 1:1 ratio (0.2 M each) was irradiated for an half an hour using Osram UV-Visible photo lamp. Color of the mixture has been changed from red to orange. The mixture was then concentrated on a water bath and then cooled to room temperature. Orange colored crystals of above mentioned photoadduct were obtained, which has been then dried in an oven to a constant yield.

Prepared photoadduct was milled in PM 100 planetary high energy ball mill to reduce its size using 20 balls of 5 mm. Machine has been kept for 500 rpm speed for the period of 24 h. Fixed milling time of 24 h with an interval of half an hour resulted into the size reduction of synthesized photoadduct to nano size which has been confirmed from XRD. The photoadduct formed was subjected to different spectroscopic and surface characterization techniques.

2.3. Synthesis of PTh/$[Fe(CN)_3(NO)(bpy)] \cdot 4H_2O$ nanocomposite fibers

Pure PTh has been synthesized as per the literature [11]. Nanocomposite fibers have been synthesized by in-situ oxidative chemical polymerization in non-aqueous medium. Following procedure has been used for the preparation of PTh/$[Fe(CN)_3(NO)(bpy)] \cdot 4H_2O$ nanocomposite

fibers: 1 g of the prepared photoadduct crystals have been dispersed in the 0.30 molar solution of thiophene in $CHCl_3$ (70 ml) for about 15 minutes using a magnetic stirrer. To this mixture was then added slowly the equimolar solution of $FeCl_3$ as oxidant (in 180 ml of $CHCl_3$). Temperature has been kept in the range of 10-15ºC. During continued stirring for 24 hrs, black colored precipitate of nanocomposite fibers have been obtained which were washed thoroughly with $CHCl_3$ and CH_3OH. During washing black color of the precipitate has been changed to brown. This was then dried in oven at 70°C. The schematic representation for the synthesis of nanocomposite fibers have been illustrated in scheme 1 and has been described in section 3.6.

3. Results and Discussion

3.1. Elemental Analysis

Based on the observed percentage from CHN analysis (C: 39%, H: 3.4%, N: 23%) and EDX (Fig. 1), the empirical formula assigned to the synthesized photoadduct was found to be $[Fe(CN)_3(NO)(bpy)]\ 4H_2O$. The calculated percentage obtained from the above formula was found to be 13.8% (Fe), 19% (O), 39.8% (C), 4.0% (H) and 21.4% (N) which is in good agreement with the observed values. Hence the above formula is a rigorous formula for the photoadduct formed.

3.2. UV-Visible characterization

UV-Visible spectrum observed from 190 to 700 nm for Sodium pentacyanonitrosylferrate(II) dihydrate before and after irradiation with 2,2-bypyridyl ligand is shown in Fig. 2a. Before irradiation, spectra show a very small absorption peak at 400 nm called Q-band and an absorption edge nearly at 305 nm called Soret or B-band. These are attributed to the following assignments: 6e→7e (Q-band, d→π*NO) and 2b$_2$→8e (B-band, d→π*CN) respectively [12].

After irradiation Q-band has been observed at nearly same wavelength (404 nm), however there is a considerable shift with regard to B-band from 305 to 260 nm having a shoulder. Such a shift in the B-band describes the CN ligand exchange instead of NO as this band corresponds to d→π*CN transition, justifying the formation of photoadduct. This result is in accordance with the FTIR spectra. Quantitatively crystal field stabilization energy (Δ) of complex before and after irradiation was found to be 298 KJ/mole and 295 KJ/mole respectively. Decrease in Δ_o justifies CN^- exchange with 2,2-bypyridyl since former being more pi-accepting than 2,2-bypyridyl.

Optical band gap determination is essential to assess the electrical and optoelectronic properties of materials. This band gap for the complex before and after irradiation is obtained using Tauc relationship [13].

$$\alpha h\upsilon = A(h\upsilon - E_g)^n$$

Where α is the absorption coefficient, υ is the frequency, factor A depends on transition probability and is supposed to be constant within the optical frequency range (an energy independent constant). n is the index describing the electron transition process and is related to density of states. It possesses discrete values viz 1/2, 3/2, 2 & 3 for direct allowed, direct forbidden, indirect allowed and indirect forbidden transitions respectively. From the plot of $(\alpha h\upsilon)^n$ vs. $h\upsilon$, linear fit is obtained for n=1/2, for the complex before irradiation indicating the transition to be direct allowed, and for n=2 for the complex after irradiation indicating the transition to be direct forbidden as shown in Fig 2b. By extrapolating $(\alpha h\upsilon)^n = 0$, band gap obtained before and after irradiating complex and 2,2-bypyridyl is found to be 3.8 eV and 5.1 eV respectively. This value of optical band gap shows dielectric nature of material and is

suitable material for optoelectronic applications. Increase in band gap to 5.1 eV (after irradiation) from 3.8 eV (before irradiation) is ascribed to the perturbation of energy levels owing to the formation of photoadduct.

Moreover, both depict a wider transparency in the most part of visible region which is an essential condition for the material to show NLO properties. The wavelength cutoff for complex before irradiation is around 305 nm while that after irradiation, it is around 260 nm, suggesting the suitability of material (photoadduct) for second harmonic generation (SHG) of the 1064nm Nd: YAG laser radiation. Refractive index (μ) and reflectance (R) are calculated for photoadduct using Reddy and Anjaneyulu relationships that correlates band gap with refractive index [14]:

$E_g \exp(\mu) = 36.3$ &

$R = [(\mu-1)/(\mu+1)]^2$

The calculated values for μ and R are found to be 1.96 and 0.105 respectively. This shows the high value of refractive index and low value of reflectance which indicates more transparency of material to visible radiation.

3.3. Second Harmonic Generation (SHG) test

As the photoadduct exhibits complete transmittance in the visible part of electromagnetic spectrum, it is therefore imperative to conduct SHG test for its nonlinear optical behavior. Second harmonic generation of the synthesized photoadduct was evaluated by the Kurtz and Perry powder technique. The powered photoadduct was packed in a microcapillary of uniform bore and was exposed to laser radiation. A Q-switched Nd-YAG laser beam of fundamental

wavelength 1064 nm (8 ns pulsed width and 10 Hz pulse rate) was made to fall normally on the sample cell. The emitted light was focused by a lens and detected by the photomultiplier tube, a green emission of wavelength 532 nm was observed which confirmed the generation of second harmonics. During the experiment, KDP was used as reference. It is observed that the SHG efficiency of the present photoadduct sample is 0.63 times that of KDP.

3.4. FTIR Characterization

FTIR spectra of, 2,2-bypyridyl, Photoadduct, PTh and Nanocomposite is shown in Fig. 3. Sodium pentacyanonitrosylferrate(II) dihydrate exhibit vibrational frequencies at (2178, 2143, 2083), 1945, 666 and 433-417 cm^{-1} which have been assigned to the characteristic stretching frequencies of -C≡N, -NO, Fe-NO and Fe-CN respectively [15]. 2,2-bypyridyl on the other hand depict peaks at 3000-3400, 1608, 1557 and 756 cm^{-1} which are ascribed to C-H stretching vibrations, C=C stretching, C=N vibrations and H-out of plane bending respectively [16]. Formation of photoadduct by photochemical irradiation of Sodium pentacyanonitrosylferrate(II) dihydrate with 2,2-bypyridyl ligand is justified as the peaks due to 2,2-bypyridyl also exhibit their appearance in the photoadduct but have undergone shifts. C-H stretching vibrations coupled with H_2O peaks, C=C stretching and C=N vibrations of 2,2-bypyridyl are observed in the photoadduct at 3400-3600, 1617, 1447 cm^{-1} respectively. Moreover, two among the three CN vibrations (axial and equatorial CN ligands) occur with reduced or negligible transmittance which indicates the replacement of two CN ligands, rather than NO ligand since its vibrational peak is well-defined at 1923 cm^{-1}, by a bidentate 2,2-bypyridyl ligand. The peak at 517 cm^{-1} in the photoadduct is due to the Fe-N stretching vibration of coordinated 2,2-bipyridyl.

In the stretching vibrational region of PTh, the peaks of 2900-3400 cm^{-1} and 1630 cm^{-1} can be attributed to the C-H stretching vibrations and C=C characteristic peak, respectively. In its finger print region, the IR absorption peaks at 725 cm^{-1} is ascribed to the C-H out-of-plane stretching vibration of thiophene ring, which confirms the polymerization of thiophene monomer. Vibrational mode at 1034 cm^{-1} is ascribed to C-H in-plane bending vibration [17]. The FTIR of nanocomposite [Fig 3d] shows the corresponding peaks of PTh in it in addition to the peaks due to photoadduct. The C-H stretching and –OH stretching of embedded water molecules, C=C characteristic peaks and C-H in plane bend can be identified in the nanocomposite at 3400 cm^{-1}, 1629 cm^{-1}, and 1019 cm^{-1} respectively. Vibrational modes at 2179 cm^{-1} and 1964 cm^{-1} in the nanocomposite are respectively due to -C≡N and –N=O of the inserted photoadduct. This illustrates the successful synthesis of nanocomposite. Peak at 1317 cm^{-1} and 719 cm^{-1} in nanocomposite is attributed to the C=N vibrations of coordinated 2,2-bypyridyl and C-H out of plane stretching vibrations of 2,5-coupled thiophene rings respectively .

From the above discussion successful synthesis of photoadduct and its nanocomposite with PTh is proved.

3.5. X-ray Diffraction (XRD)

Fig. 4 shows the X-ray diffraction of photoadduct and its nanocomposite with PTh. It is evident that photoadduct exhibits strong intense peaks, thereby illustrating its crystalline nature. These peaks have been indexed using powder-X which depicts an orthorhombic structure of photoadduct with a space group of pnnm. This matches well with the JCPDS-International Centre for diffraction data, file no. 84-1381. Also, nanocomposite shows the well-defined diffraction peaks which are characteristic of photoadduct. This indicates the

insertion of photoadduct particles in PTh matrix for the formation of nanocomposite. These results are in good agreement with the TEM results as it clearly depicts a two phase system consisting of photoadduct particles in PTh matrix. The lattice parameters obtained after refinement and volume of unit cell for both photoadduct and nanocomposite are almost same as shown in Table 1. Crystallite size of photoadduct and nanocomposite obtained using Scherrer formula was found to be 25.5 and 71.1 nm respectively. This increase in crystallite size of nanocomposite is owing to the agglomeration of photoadduct particles as is clear from the TEM micrographs.

3.6. SEM and TEM Characterization

Surface morphology of PTh, photoadduct and nanocomposite is entirely different as shown in Fig. 5(a-c). SEM image shows rough surface of PTh and exhibits high degree of porosity making it less dense. Photoadduct on the other hand shows high density and compactness since particles are closely packed. This suffices to conclude that particles are in nano size which is confirmed from X-ray diffraction. However few dislocation networks are observed on its surface and a small crack of low depth is seen. This may be owing to solvent inclusions which is a commonly occurring phenomenon in solution grown crystals. Major part of material is free from defects. In nanocomposite, however, degree of porosity decreases and compactness increases due to the insertion of photoadduct. This justifies the formation of nanocomposite.

Fig. 5(d-e) shows TEM images of samples. Photoadduct depict rhombus like crystals. Nanocomposite on the other hand clearly shows a two phase system consisting of polythiophene chains and photoadduct particles. In this, the PTh chains adopted fiber like structure in which are the photoadduct particles dispersed as is clearly visible in its TEM

micrograph, however they are somewhat agglomerated owing to which size has been found to increase as evidenced by X-ray diffraction.

The proposed mechanism for this is illustrated in Scheme 1. In this mechanism, it is proposed that there occurs the formation of polythiophene nuclei, which look like threads, over which are both the monomer units as well as the photoadduct particles. During continued stirring, these monomer units further polymerize to form polythiophene fibers, which develop vanderwaals type interaction with one another to form bundles of fibers, engulfing the photoadduct particles and hence lead to the formation of nanocomposite. Due to this vanderwaals interaction between polymer threads, nanocomposite appears to be more compact and dense than pure PTh as is reflected by SEM image. Furthermore, agglomeration of photoadduct particles may be attributed to strong polymer-polymer interaction as compared to polymer-photoadduct interaction.

3.7. Thermogravimetry and Differential Scanning Calorimetry

Thermogravimetry (TG) is a technique for measuring the change in weight of substance owing to dehydration, decomposition and oxidation as a function of temperature or time. Differential scanning calorimetry (DSC) on the other hand is a thermo analytical technique in which difference in the amount of heat between sample and reference is measured when a thermal event occurs so as to maintain them at a constant temperature during the heating programme. The machine used for this purpose is SDT Q600 V8.3 Build 101 instrument. The thermogram of synthesized photoadduct and nanocomposite performed at constant heating rate of 10°C min^{-1} in N_2 atmosphere are shown in Fig. 6(a,b). Photoadduct shows four transitions. The first transition occurs from ambient to 161ºC with an observed weight loss of

12% against the calculated weight loss of 12.5% involves the loss of three moles of lattice water whose presence is already confirmed from FTIR. Thermogram runs parallel till 217ºC where from second decomposition takes place with a weight loss of 26.08% against the calculated weight loss of 25% up to 341ºC, this is attributed to the decomposition of 2,2-bypyridyl and the expulsion of one mole of H_2O. Third decomposition occurs up to 451ºC with a weight loss of 12.32% against calculated weight loss of 13% is due to the loss of two mole of CN, thereafter the weight remains constant till 508°C where from the fourth decomposition takes place which ends at 608°C with a weight loss of 5.47% against the calculated weight loss of 6%. This is attributed to the loss of one mole of NO. The residue left at the end of temperature scan is around 45%. DSC also shows four transitions corresponding to TG transitions. The first and last transitions in the DSC scan are endothermic which are attributed to the dehydration and decomposition of an otherwise stable product. The middle two transitions are exothermic involving large evolution of heat. This has been attributed to the decomposition of a less stable photoadduct after it dehydrates to form some stable product. The thermogram of pure PTh shows two transitions, first one arises from ambient to 160°C with a weight loss of about 18 % as soon as it is subjected to heating, which is ascribed to the loss of moisture and dopant molecules. However an abrupt decomposition of 60.69 % occurs within a narrow temperature range of 234–300°C occurs which is attributed to the large scale thermal degradation of PTh chains thereby exhibiting its limited thermal stability. The residue left at the end is approximately 20 % [18].

Incorporation of photoadduct in PTh matrix to form nanocomposite is justified since an increase in the thermal stability of PTh is observed. This is because after the removal of moisture by first transition, the second transition commences at around 300°C and ends at

390°C in contrast to that of pure PTh which starts at 234°C. Thus a shift in the decomposition temperature of around 66°C is observed from pure PTh to that of nanocomposite. This increased thermal stability of nanocomposite has been attributed to the firm held of polymer chains by photoadduct particles. Also the residue left at the end is around 30% which is higher than that of PTh.

3.8. Dielectric Study

Conducting polymers have the added advantage of possessing unique EMI shielding mechanism of reflection and absorption rather than dominated reflection for metals and carbons. This is due to their ability to regulate electrical conductivity by controlling parameters like oxidation state, doping level, morphology and chemical structure. Such a change in electrical conductivity, either the increasing or the decreasing trend, helps in EMI shielding. This is because the primary mechanism of EMI shielding is reflection from the front face of the shield, for which the shield must possess mobile charge carriers (electrons and holes) that can interact with the electromagnetic fields to cause ohmic (heating) losses. As a result shield needs to be electrically conducting. The secondary mechanism is absorption for which shield needs to possess electric and/or magnetic dipoles which can interact with electromagnetic fields to cause electric and magnetic losses. The third mechanism is multiple reflections within the shield which can affect the EMI shielding depending upon the thickness and skin depth of the shield [19]. Keeping this into consideration, the nanocomposite has been subjected to dielectric study so as to analyze suitability of nanocomposite synthesized for electronic applications.

Fig. 7a shows the variation of real (ε') and imaginary (ε'') part of dielectric constant with frequency of applied alternating field. It is evident that the dielectric constant exhibits a

normal dispersion behavior with frequency. At low frequency, the value of dielectric constant is very high, of the order of 10^5, which is due to the presence of all types of polarizations in the material viz interfacial (space charge), dipolar, ionic and electronic polarizations. With increase in frequency, dielectric constant commences to decrease rapidly which is attributed to the inability of polarizations to follow the applied filed. This dielectric dispersion can be explained on the basis of Koop's theory, based on the Maxwell-Wagner model for the heterogeneous structure of present nanocomposite material. According to this model, the dielectric material consists of two layers or phases which differ from each other in conductivity and dielectric constant. In such materials, mobility of charge carries occurs more easily and randomly through one phase and therefore is constricted at phase boundaries wherein they get trapped at the interfaces of the multiphase material with different conductivity thereby giving high value to dielectric constant at low frequencies which is of the order of 10^5. This high value of dielectric constant at low frequencies can provide absorptive mechanism to EMI shielding owing to the presence of electric dipoles which can interact with the electromagnetic radiation to cause electric losses due to which the amplitude of the incident radiation is reduced. As the frequency increases, the space charge carriers in a dielectric do not acquire a finite time to line up their axes in the direction of an applied alternating field, as a result dielectric constant decreases. At higher frequencies, even the charge clouds cannot change their skewing direction fast enough to respond to field, so ε' decreases further and hence attains a minimum and a constant value which is then independent of frequency. The decrease in the value of ε'' with frequency can be attributed to the predominance of dc-conduction contribution in the material, characterized by $\varepsilon''_{dc} =$

$\sigma_{dc}/\varepsilon_o\omega$ i.e. varies with angular frequency as ω^{-1} and without having any characteristic peak in the loss curve.

This is justified from the plot of $\ln\varepsilon''$ vs $\ln\omega$ which shows a straight line as per the relation $\varepsilon'' = A\,\omega^m$, where A is a constant. The slope of fitted curve was found to be -0.82, which is very close to -1 indicating dc-conduction dominant in the material [Fig. 7c]. Absence of relaxation peak in ε'' spectra may be due to masking of relaxation processes by electrical conduction processes [20].

Fig. 7b shows the variation of dielectric loss or dissipation factor ($\tan\delta$) and ac-conductivity (σ_{ac}) with applied alternating field. Dissipation factor exhibits a decreasing trend with increasing frequency. At low frequencies, there occurs high dissipation of energy which may be due to the dc-conduction losses in the material and at high frequencies; the nanocomposite material behaves virtually a lossless material. This may be attributed to the use of energy of applied alternating field in increasing ac-conductivity of nanocomposite material, thereby decreasing loss. Plot of ac-conductivity reveals that below 10^3 Hz, it is independent of frequency indicating dc-conductivity dominant in the material. Frequency dependence after 10^3 Hz shows ac- conductivity behavior, which shows an exponential increase with increasing frequency of ac-field. This is justified since at higher frequencies, the value of exponent s from the plot of $\ln\sigma_{ac}$ vs $\ln\omega$ as per the relation $\sigma_{ac} = A\omega^s$, was found to be 0.22 which is in between 0-1. This therefore suggests that the conduction phenomenon in the nanocomposite is the ac-conduction, which has been attributed to the hoping of charge carriers along the polymer chain [21]. Ac-conductivity of the nanocomposite material is very high and is of the order of 10^{10} S/m. This high value of ac-conductivity at high frequencies can provide reflective mechanism to EMI shielding. This is because shielding efficiency due to reflection

losses depends upon the unit power of conductivity (σ) than due to absorption losses which depends on the square root of conductivity ($\sigma^{1/2}$). This clearly shows the dominance of reflective mechanism to EMI shielding with increasing conductivity [22].

Since dielectric loss spectra do not show any relaxation peak, it is difficult to distinguish between the interfacial polarization and intrinsic relaxation contributions. However, for materials whose loss spectra exhibit a dc conduction phenomenon the dielectric spectra can be analyzed using the complex electric modulus formalism given by McCrum [23]. The complex electric modulus is expressed as the reciprocal of complex dielectric permittivity as:

$$M^* = 1/\varepsilon^* = M' + iM''$$

Where M′ and M″ are the real and imaginary components of the electric modulus. Plot of M′ and M″ vs frequency and M″ against M′ is shown in Fig. 7d. It is evident that value of M′ is zero at low frequencies thereby suggesting that the electrode polarization gives negligible contribution of M′ and hence can be ignored when permittivity data is expressed in this form. Moreover, this behavior can be explained by the lack of restoring force governing the mobility of charge carriers under the influence of electric field. This supports long range mobility of charge carriers corresponding to the dc-conduction [24]. This is justified since nanocomposite exhibit fiber like structure as shown by TEM with long polymer chains along which the charge carriers are mobile. Further an increase in the value of M′ with increasing frequency is a suggestive of short range mobility of charge carriers which correspond to the ac-conduction. Plot of M″ vs frequency exhibit similar behavior. Since the relaxation occurs at higher frequency which shows shorter relaxation time for conduction. The low frequency side of relaxation curve indicates facile hopping from one site to another than at high frequency side wherein charge carriers are spatially confined to their potential wells and hence cause short

range mobility. The relaxation curve represents the transition from long range to short range mobility of charge carriers with increasing frequency. Moreover, relaxation at higher frequency has been associated with the contribution of capacitance to the grain phase of the material [25]. Also Cole-Cole plot in terms of modulus formalism shows one single semicircular arc as shown in Fig. 7e, which also indicates the presence of one relaxation [26]. Impedance spectroscopy is a very convenient and powerful experimental technique that enables us to correlate the dielectric properties of a material with its microstructure, and helps to analyze and separate the contributions from various components (i.e., through grains, grain boundary, interfaces, etc.) of polycrystalline materials over wide frequency range. In order to distinguish between the contribution from grain and grain boundary, complex impedance plots (Cole–Cole plots) were obtained by plotting the real (Z′) part corresponding to the imaginary part (Z″) as is shown in Fig. 7f. The plot depicts one semicircle, corresponding to the resistance of around 216 Ω and capacitance of 3.36×10^{-9} F which has been attributed to the grain boundary resistance and capacitance respectively. Resistance obtained is comparatively a lower value of resistance and is justified as the ac-conductivity of the nanocomposite is very high for such a material.

3.9. Photocatalytic Activity

Photocatalytic activity of nanocomposite fibers have been compared with PTh and in the presence of scavengers like disodium salt of EDTA and *t*-butyl alcohol as shown in Fig. 8. Fig. 8a reveals 87% photo-degradation in the presence of nanocomposite as photocatalyst than for the pure PTh which is around 66% after 3 hours of irradiation. Moreover, this material, when compared with the commercial P25 benchmark photocatalyst, showed enhanced photocatalytic activity since P25 depict only about 40% degradation of MO dye as compared

to our system which shows around 87%. This clearly shows the superiority of the present system for photocatalysis. This also has the higher photodegradation than many other materials as reported in the literature (see references in Table 2). This enhanced photo-degradation of MO dye by nanocomposite is expected to be because of (1) porous nature of nanocomposite as indicated by its SEM image, (2) small size of particles due to which surface to volume ratio considerably increases which leads to more adsorption of dye for degradation, (3) the significant charge separation of photoinduced electrons and holes through the electronic interaction between photoadduct particles and PTh fibers and (4) the development of hetero junctions.

To account for the actual reasons, BET for the surface area determination and photoluminescence (PL) for the recombination mechanisms have been carried out. It is observed that BET surface area has been found to be 26.1, 18.9 and 8 m^2/g for photoadduct, nanocomposite fibers and pure PTh respectively. This is in accordance with the particle sizes of photoadduct and nanocomposite as shown by XRD. Decreasing surface area from photoadduct to nanocomposite is because of the increasing particle size, which clearly shows the impact of PTh matrix. This is also clear from the adsorption of MO dye in dark which reflects nearly 13% adsorption as shown in Fig. 8b. On comparing the surface area of nanocomposite fibers (18.9 m^2/g) with the commercial P25 benchmark (45 m^2/g), it is of lower value therefore does not seem to be much impressive to enhance photocatalytic activity. Another factor to consider is the development of interface contact which can lead to increased separation of charge carriers to enhance photocatalytic activity. For this purpose PL measurement has been carried out as is shown in Fig. 8c. PL of photoadduct exhibit a high intensity emission at around 325 nm under the excitation wavelength of 280 nm. This has

been attributed to the metal to ligand charge transfer transition. PTh on the other hand shows negligible emission which is because of the density of states and easy migration of charge carriers along the polymer chain thereby leading to non-radiative transitions. In nanocomposite fibers, however, the emission spectra is of reduced intensity. This shows the impact of PTh matrix on the PL of photoadduct. In this, PTh matrix acts as quencher to prevent the electron-hole pair recombination. The possible mechanism can be the formation of a hetero junction between PTh and photoadduct particles with matching band potentials, due to which there occurs easy transfer of energy via the movement of electrons and holes. This energy transfer leads to a significant separation of charge carriers thereby prolonged their life time, which is an essential condition for photocatalysis. The proximal interface contact between photoadduct and PTh chains can be owing to (1) dimensionality effect as there is a rhombus like photoadduct crystals-PTh fibers (3D-1D) composite system [33] and (2) by surface charge modification process since Fe^{3+} ions from oxidant can get adsorbed on the photoadduct particles due to chemical similarity. This leads to the development of positive charge on photoadduct particles which can therefore have interaction with the S atoms of polythiophene chains thereby increasing surface contact.

Since degradation of an organic dye solution occurs by oxidizing it. Therefore it is imperative to identify the main oxidant species in the photocatalytic action of nanocomposite for dye degradation. This will also help us to understand the mechanism of action. The proposed mechanism for dye degradation involves the simultaneous excitation of electrons from HOMO to LUMO of PTh (band gap 2.1 eV) and from valance band (VB) to conduction band (CB) in case of photoadduct, inspite of having the high band gap of photoadduct. This is because the lamp used in the present study is a Xe-arc lamp which emits a broad spectrum

from 200 to 2500 nm. Band gap of 5.1 eV correspond to the wavelength of 243 nm, hence can therefore be stimulated by light. Such a photo-generated electrons of PTh migrate to the CB of photoadduct and holes from the VB of photoadduct to the HOMO of PTh as PTh is not only electron donor but also the hole acceptor and possess greater mobility of charge carriers, thus leads to synergism between photoadduct and PTh fibers. This is schematically shown in scheme 2. Consequently, owing to this synergistic effect, the life time of the charge carriers over the photocatalyst (nanocomposite) is prolonged, which in turn causes the formation of reactive oxygen species (ROS) with strong oxidizing ability. The ROS produced include hydroxyl radicals, $OH^{\bullet}$ and superoxide radicals, $O_2^{\bullet -}$ which therefore cause the degradation of MO dye. To confirm such oxidants for dye degradation, photocatalytic activity of nanocomposite has been carried out in the presence of scavengers which include disodium salt of EDTA (EDTA-Na_2, hole scavenger) and t-butyl alcohol (electron scavenger) [34]. It is observed that the photocatalytic activity of nanocomposite is considerably decreased as shown in Fig. 8d. 87% of MO degradation after 3 hr of irradiation is because of the easy migration of charge carriers between PTh and photoadduct. However in the presence of disodium salt of EDTA and t-butyl alcohol (1mM each) as electron and hole scavengers respectively, the rate of MO degradation over nanocomposite has been decreased to 60% and 30% respectively. This has been attributed to the abortion of easy mobility of charge carriers between PTh and photoadduct, thereby affects the synergism.

Kinetic studies of the MO degradation have also been carried out in which the photo-degradation rates fits second order kinetics well, as observed from the straight line plot of $1/C_t$ against irradiation times (t) using the integrated rate expression for second order reaction:

$1/C_t - 1/C_o = kt$

Where C_o is the initial concentration of MO dye, C_t is the concentration of MO dye at different irradiation times and k is the observed second order rate constant. From the plot as shown in Fig 8e, slope of the straight line gives the observed rate constant (k) for the degradation of MO dye which has been found to be $7^x 10^{-4}$ Lmol^{-1}s^{-1} and the intercept gives the initial dye concentration which comes out to be same as has been actually taken i.e., 50 ppm. This justifies the second order kinetics.

3. Conclusion

Preparation of photoadduct has been carried out by a photochemical route and has been subjected to size reduction by high energy ball mill. Empirical formula of the photoadduct was found to be [Fe(CN)$_3$(NO)(bpy)] 4H$_2$O. This has been then used as filler in PTh matrix for the formation of nanocomposite fibers by in-situ technique. UV-Visible, FTIR, SEM, TEM and XRD proved the successful synthesis of photoadduct and its nanocomposite. UV-Visible spectra exhibited increased band-gap of photoadduct than SNP. From TG/DSC, increase in thermal stability and rigidity of nanocomposite has been observed. Dielectric studies showed a capacitive effect at low frequencies and a very high ac-conductivity of the order of 10^{10} S/m. This high value of ac-conductivity can provide reflective mechanism to EMI shielding. Modulus formalism showed dc-conduction mechanism at low frequencies suggesting long range mobility of charge carriers owing to fibrous nature as revealed by TEM. Cole-Cole impedance plot exhibit one semi-circle which corresponds to the grain boundary having a resistance of 216 Ω. Photocatalytic activity of nanocomposite is higher than that of PTh. This has been attributed to the formation of ROS like hydroxyl and superoxide radicals, which are strong oxidizing agents to cause dye degradation. This has been confirmed by the use of scavengers like EDTA-Na$_2$ and *t*-butyl alcohol which reduces the dye degradation.

Moreover, material is having lower surface area (18.9 m^2/g) than commercial P25 bench mark (45 m^2/g). Therefore the enhanced photocatalytic activity was attributed to the development of greater interface contact between PTh and photoadduct particles which has been evidenced by PL measurements. In addition kinetic study revealed the degradation to follow second order kinetics with an observed rate constant of 7×10^{-4} Lmol^{-1}s^{-1}.

Author Information

Corresponding author

*Email: haniefarf@gmail.com, phone: 09906834560

Note

The authors declare no competing financial interest.

Conflict of Interest Statement:

There is no conflict of interest between authors and the organizations in which the present work has been carried out.

References:

[1] R. Lu, L. Yuanzhi, H. Jingtao, Z. Xiujian, P. Chunzu, *ACS Appl. Mater. Interfaces,* 2014, 6, 1608-1615.

[2] D.P. Singh, *Sci. Adv. Mater.,* 2010, 2, 245-272.

[3] S.S. Ray, M. Biswas, *Synth. Met.,* 2000, 108, 231-236.

[4] J. Z. Yin, S. B. Huang, Z. C. Jian, M. L. Pan, Y. Q. Zhang, Z. B. Fei, X. R. Xu, *Appl. Phys. A*, 2015, 120, 1529–1535.

[5] X. Xie, K. Kretschmer, G. Wang, *Nanoscale*, 2015, 7, 13278-13292.

[6] M. Yang, N. Zhang, M. Pagliaro, Y. J. Xu, *Chem. Soc. Rev,*, 2014, 43(24): 8240-8254.

[7] M. Kowsar, T. Ruheena, F. S. Asma, A. Siraj, M. L. Singla, *J. Mater. Sci.: Mater. Electron*, 2009, 20, 958-966.

[8] E. Volkan, S. Fahriye, G. Handan, G. Ahmet, A. Ahmet, *Appl. Catal. B: Enviromental*, 2012, 119, 197-206.

[9] L. Yangming, L. Danzhen, H. Junhua, X. Guangcan, W. Jinxiu, L. Wenjuan, F. Xianzhi, *J. Phys. Chem. C*, 2012, 116, 5764-5772.

[10] M. H. Farzana, S. Meenashi, *Ind. Eng. Chem. Res.*, 2014, 53, 55-63.

[11] M. H. Najar, M. Kowsar, *J. Mater. Sci.: Mater. Electron.*, 2013, 24, 4332-4339.

[12] P.T. Manoharan, B.G. Harry, J. Am. Chem. Soc. 1965, 87, 15.

[13] M. H. Najar, M. Kowsar, *Synth. Met.,* 2014, 198, 76-83.

[14] P. Vasudevan, S. Sankar, S. G. Raj, *Optik*, 2013, 124, 4155-4158.

[15] M. H. Najar, M. Kowsar, *J. Mater. Sci.: Mater. Electron.,* 2015, 26, 6458-6470.

[16] N. Preda, L. Mihut, M. Baibarak, I. Baltog, M. Husanu, C. Bucur, T. Velula, *Rom. Journ. Phys.*, 2009, 54, 667–675.

[17] K. Fanhong, W. Yan, Z. Jun, X. Huijuan, Z. Baolin, W. Yanmei, W. Shurong, W. Shihua, *Mat. Sci. and Engg. B*, 2008, 150, 6-11.

[18] M. Kowsar, T. Ruheena, F. S. Asma, A. Siraj, M. L. Singla, *J. Mater. Sci.: Mater. Electron*, 2009, 20, 958-966.

[19] M. H. Al-Saleh, U. Sundararaj, *Carbon,* 2009 , 47, 1738 –1746.

[20] M. H. Lakhdar, B. Ouni, M. Amlouk, *Mat. Sci. in Semicond. Processing,* 2014, 19, 32-39.

[21] M. A. Dar, K. M. Batoo, V. Verma, W.A. Siddiqui, R.K. Kotnala, *J. of Alloys and Compd.,* 2010, 493, 553-560.

[22] P. Saini and M. Arora, *Intech Open Science Open Minds,* 2012, Chapter 3, pp 71-112.

[23] G. R. Saad, A. A. Ezz, H. A. Ahmed, *Thermochimica Acta,* 2015, 599, 84-94.

[24] J. Hazarika, A. Kumar, *Synth. Met.*, 2014, 198, 239-247.

[25] L. Singh, I.W. Kim, B. C. Sin, A. Ullah, S. K. Woo, Y. Lee, *Mat. Sci. in Semicond. Processing*, 2015, 31, 386-396.

[26] N. Tugluoglu, S. Karadeniz, B. Bar, *Mat. Sci. in Semicond. Processing*, 2014, 27, 891-898.

[27] X. T. Zhou, H. B. Ji, X. J. Huang, *Molecules*, 2012, 17, 1149-1158.

[28] A. Y. Zhang, L. L. Long, W. W. Li, W. K. Wang, H. Q. Yu, *Chem. Commun.,* 2013, 49, 6075-6077.

[29] F. Zhang, S. Yuanji, Z. Zongshan, S. Weijie, C. Yang, *Appl. Catal. B: Environmental*, 2014, 150, 472– 478.

[30] Z. Yunfeng, X. Shoubin, Y. Dan, *React. & Funct. Poly.*, 2010, 70, 282–287.

[31] Z. Yunfeng, Y. Dan, *Solar Energy Mat. & Solar Cells*, 2010, 94, 1658–1664.

[32] X. Pan, W. Lianjun, S. Xiaoqiang, X. Binhai, W. Xin, *Ind. Eng. Chem. Res.,* 2013, 52, 10105-10113.

[33] N. Zhang, M. Yang, S. Liu, Y. Sun, Y. J. Xu, *Chem. Rev.,* 2015, 115, 10307–10377.

[34] M. Khatamian, M. Fazayeli, B. Divband, *Mat. Sci. in Semicond. Processing*, 2014, 26, 540–547.

Figure Captions:

Fig. 1. EDX of the synthesized photoadduct.

Fig. 2. UV-Visible spectra of $Na_2[Fe(CN)_5NO]$ $2H_2O$/2,2-bypyridyl mixture before and after irradiation (a); Band gap determination of $Na_2[Fe(CN)_5NO]$ $2H_2O$/2,2-bypyridyl mixture before and after irradiation (b).

Fig. 3. FTIR spectra of 2,2-bypyridyl (a); $[Fe(CN)_3(NO)(bpy)]$ $4H_2O$ (b); PTh (c); PTh/$[Fe(CN)_3(NO)(bpy)]$ $4H_2O$ nanocomposite fibers (d).

Fig. 4. XRD pattern of $[Fe(CN)_3(NO)(bpy)]$ $4H_2O$ (a) and nanocomposite fibers (b).

Fig. 5. SEM images of PTh (a); $[Fe(CN)_3(NO)(bpy)]$ $4H_2O$ (b) and nanocomposite fibers (c). TEM images of $[Fe(CN)_3(NO)(bpy)]$ $4H_2O$ (d) and nanocomposite fibers (e).

Fig. 6. TG/DSC of $[Fe(CN)_3(NO)(bpy)]$ $4H_2O$ (a) and nanocomposite fibers (b).

Fig. 7. Variation of dielectric constant (ε' & ε'') (a); loss tangent and ac-conductivity (b) with frequency; plot of $\ln\varepsilon''$ vs $\ln\omega$ (c); variation of electric modulus (M' & M'') with frequency (d); Cole-Cole plot in electric modulus formalism (e) and Cole-Cole impedance plot (f) for nanocomposite fibers .

Fig. 8. Photocatalytic degradation of MO dye for PTh and nanocomposite fibers with irradiation time (a); % adsorption of MO dye with time in dark for nanocomposite fibers (b); PL spectra of photoadduct, PTh and nanocomposite fibers (c); Reduction in the degradation of MO dye in the presence of scavengers (d) and Plot of $1/C_t$ vs t following second order kinetics (e).

Scheme 1. Illustration for the growth of nanocomposite fibers.

Scheme 2. Proposed mechanism for the photocatalytic degradation of MO dye by the nanocomposite fibers.

Table 1. Geometrical parameters of photoadduct ([Fe(CN)$_3$(NO)(bpy)] 4H$_2$O) and nanocomposite fibers.

Table 2. Comparison of % photodegradation of nanocomposite fibers with commercial P25 bench mark and other materials reported against MO dye.
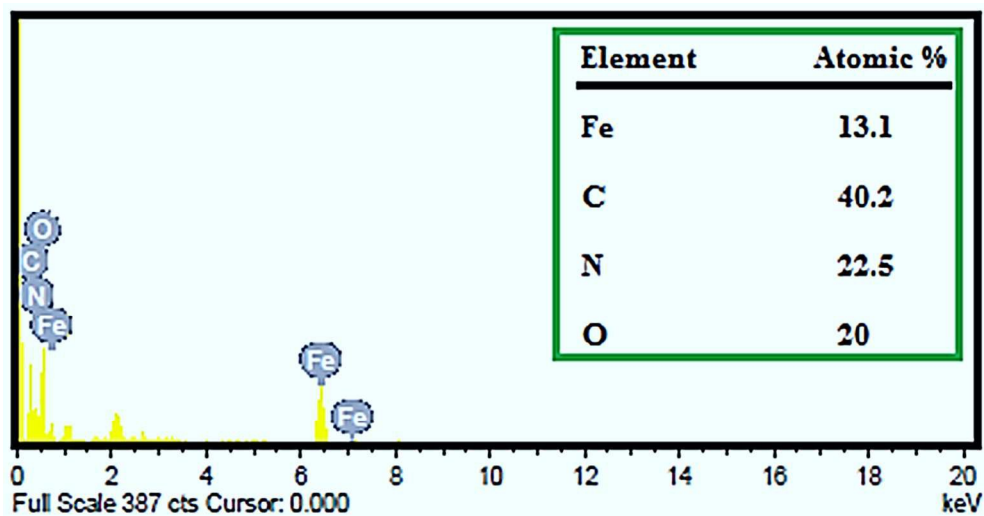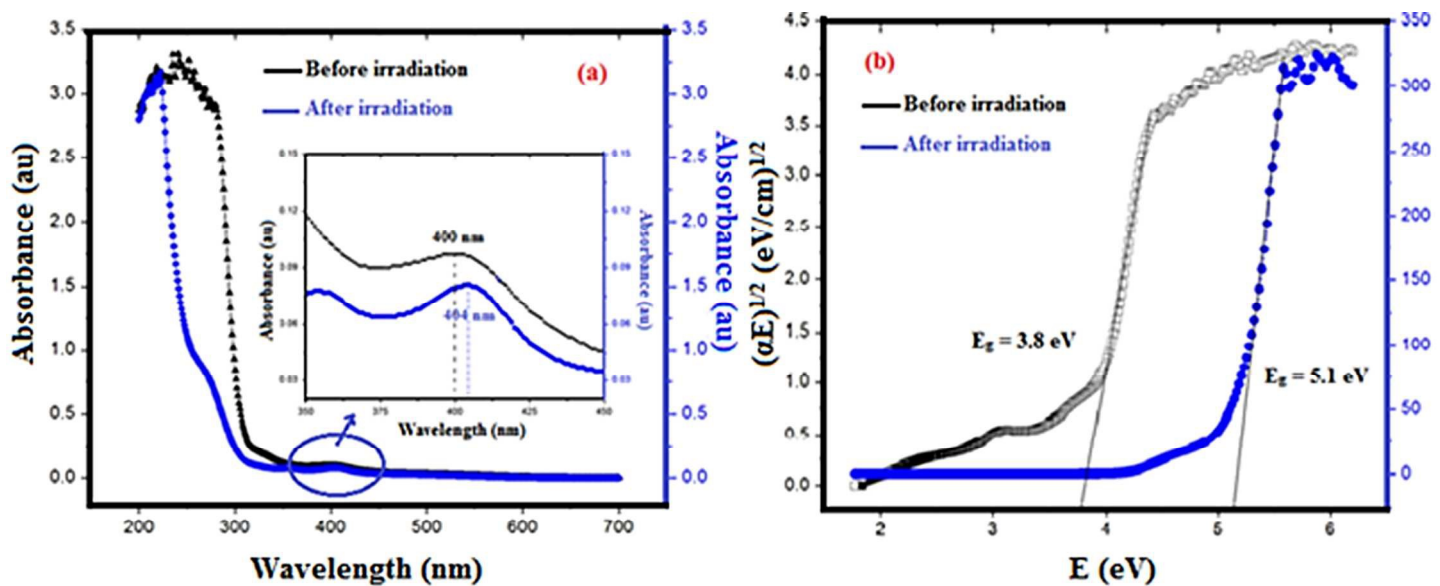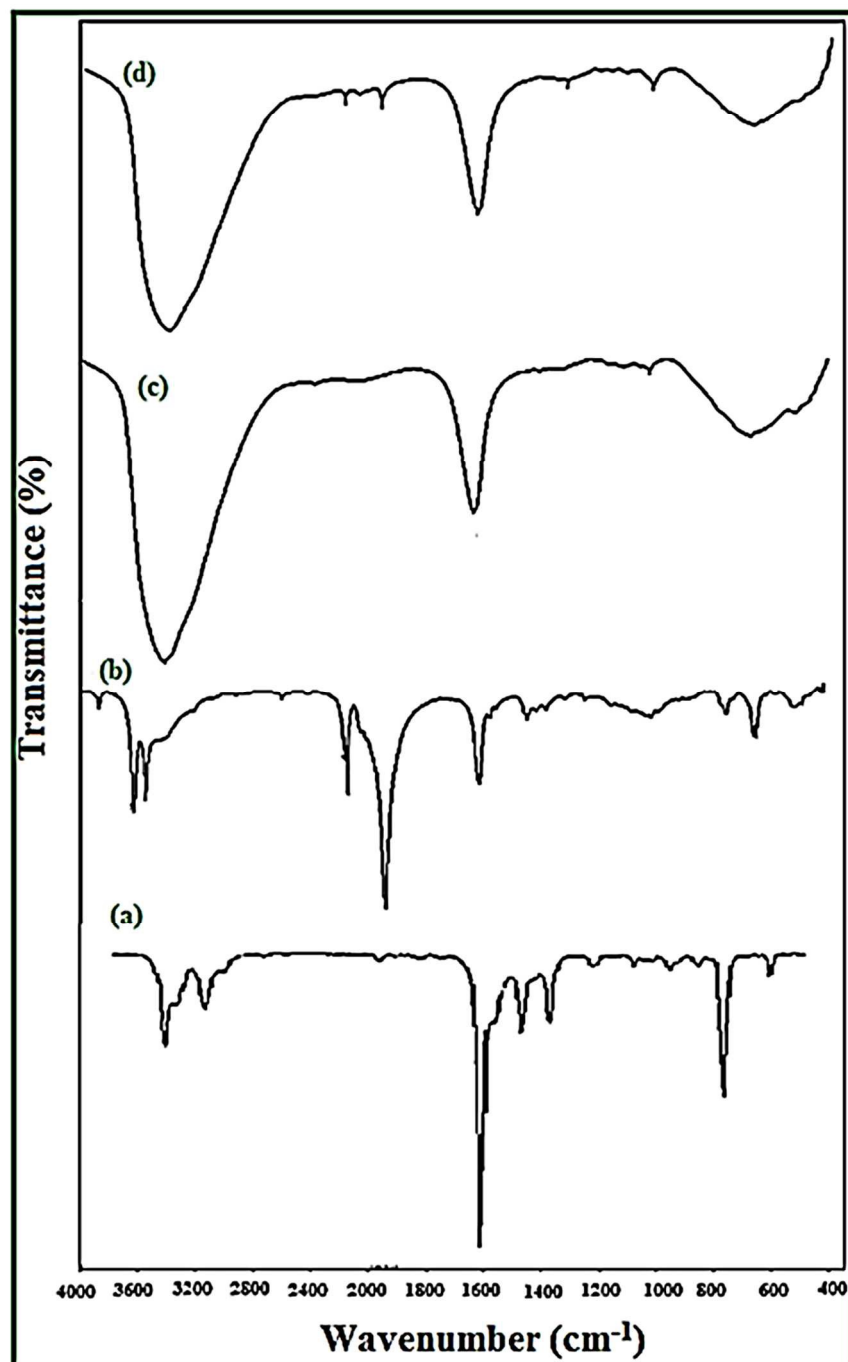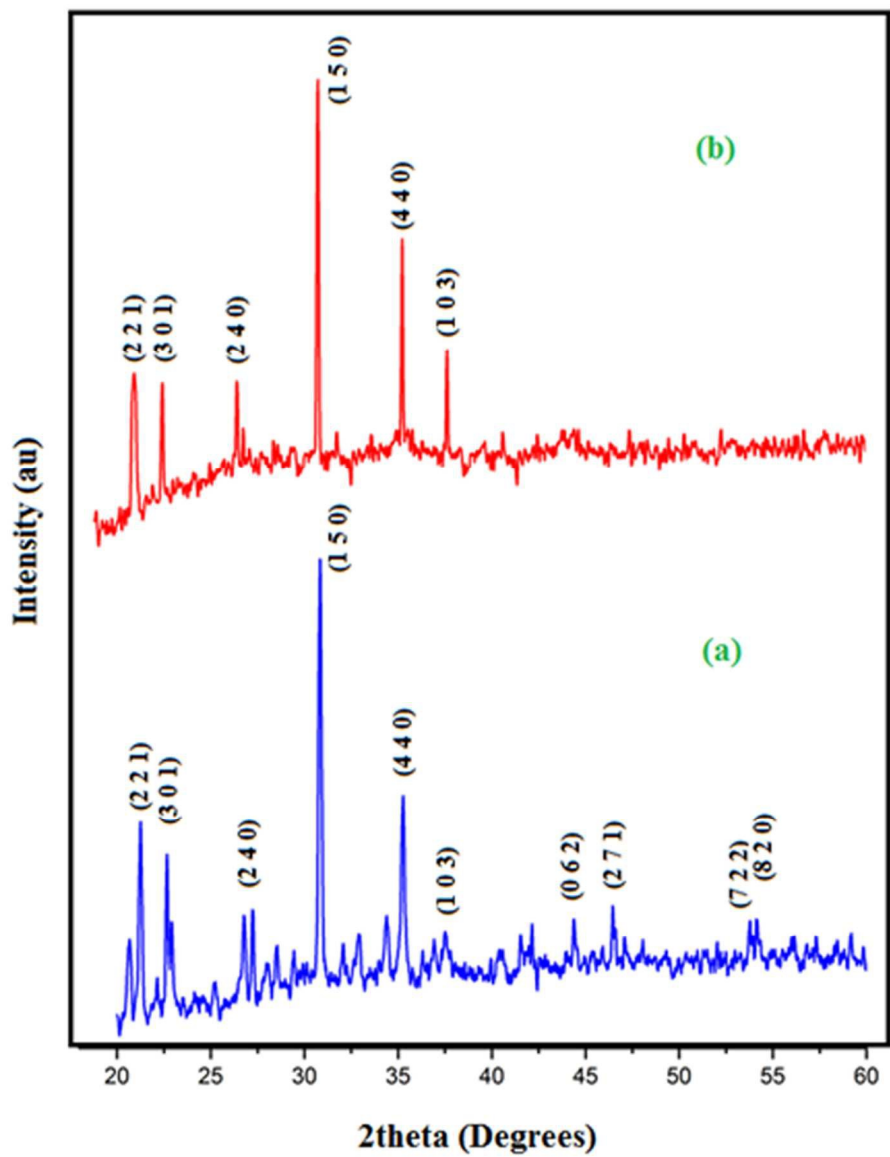
Fig. 1

Fig. 2

1

Fig. 3

2

Fig. 4

Fig. 5

Fig. 6

5

Fig. 7

6

Fig. 8

FeCl₃ Solution (Oxidant)

Nucleation

Growing

● = Photoadduct

⬠ = Thiophene (Monomer)
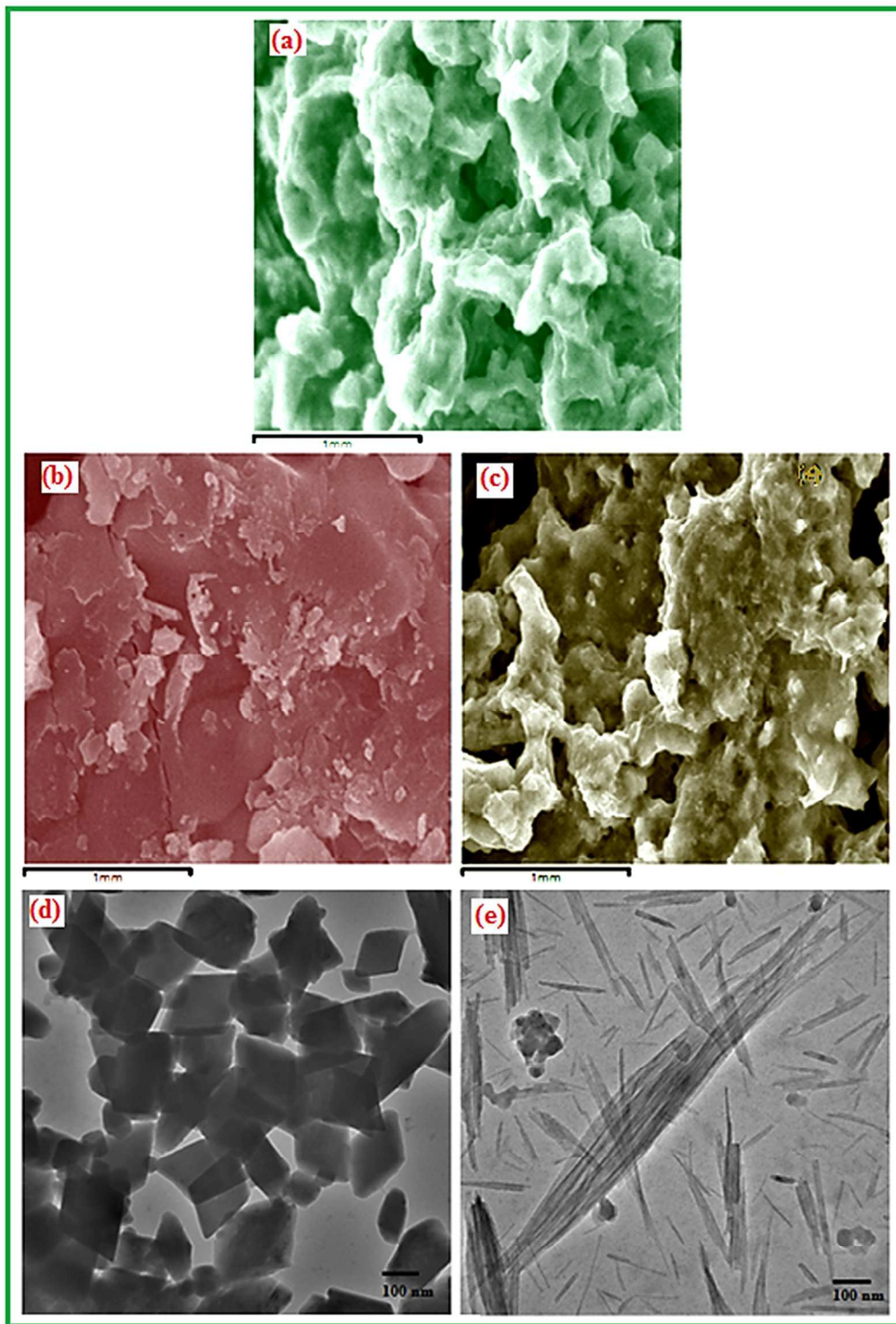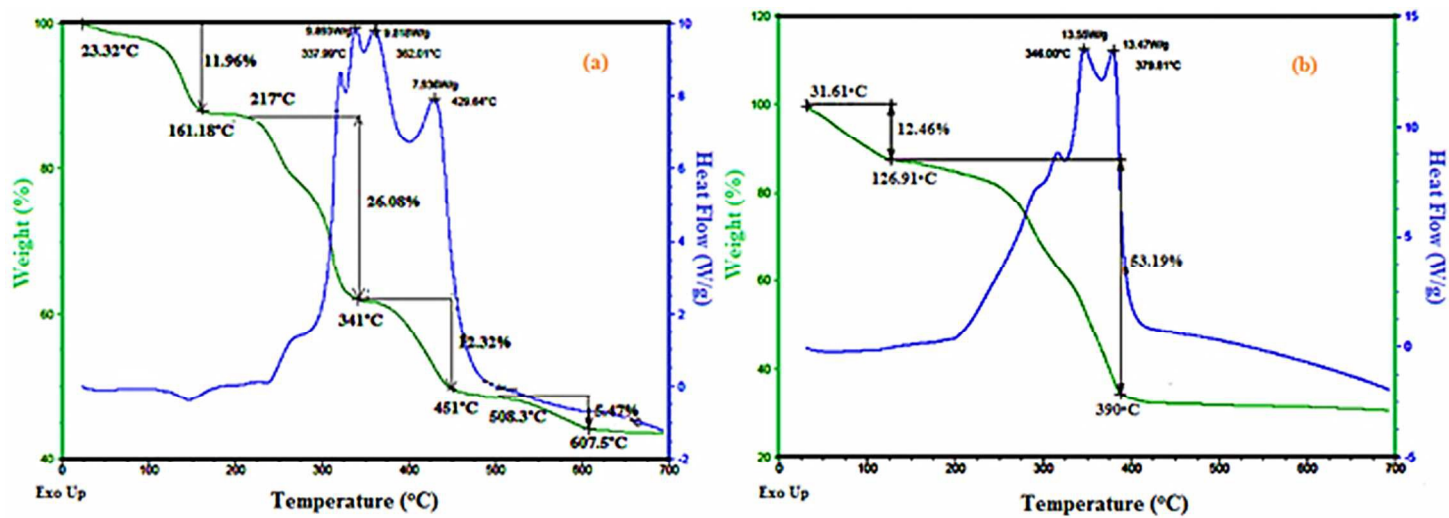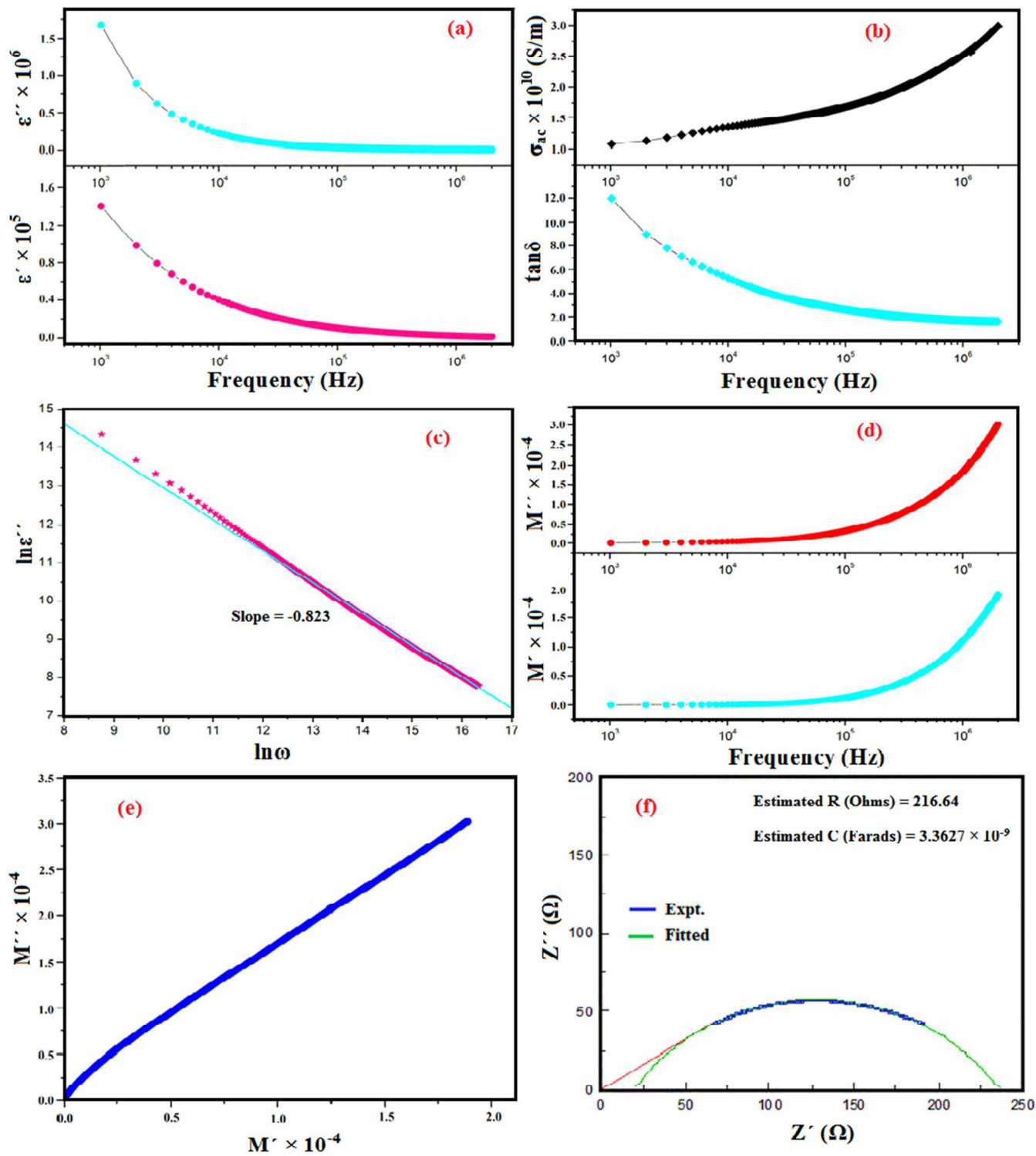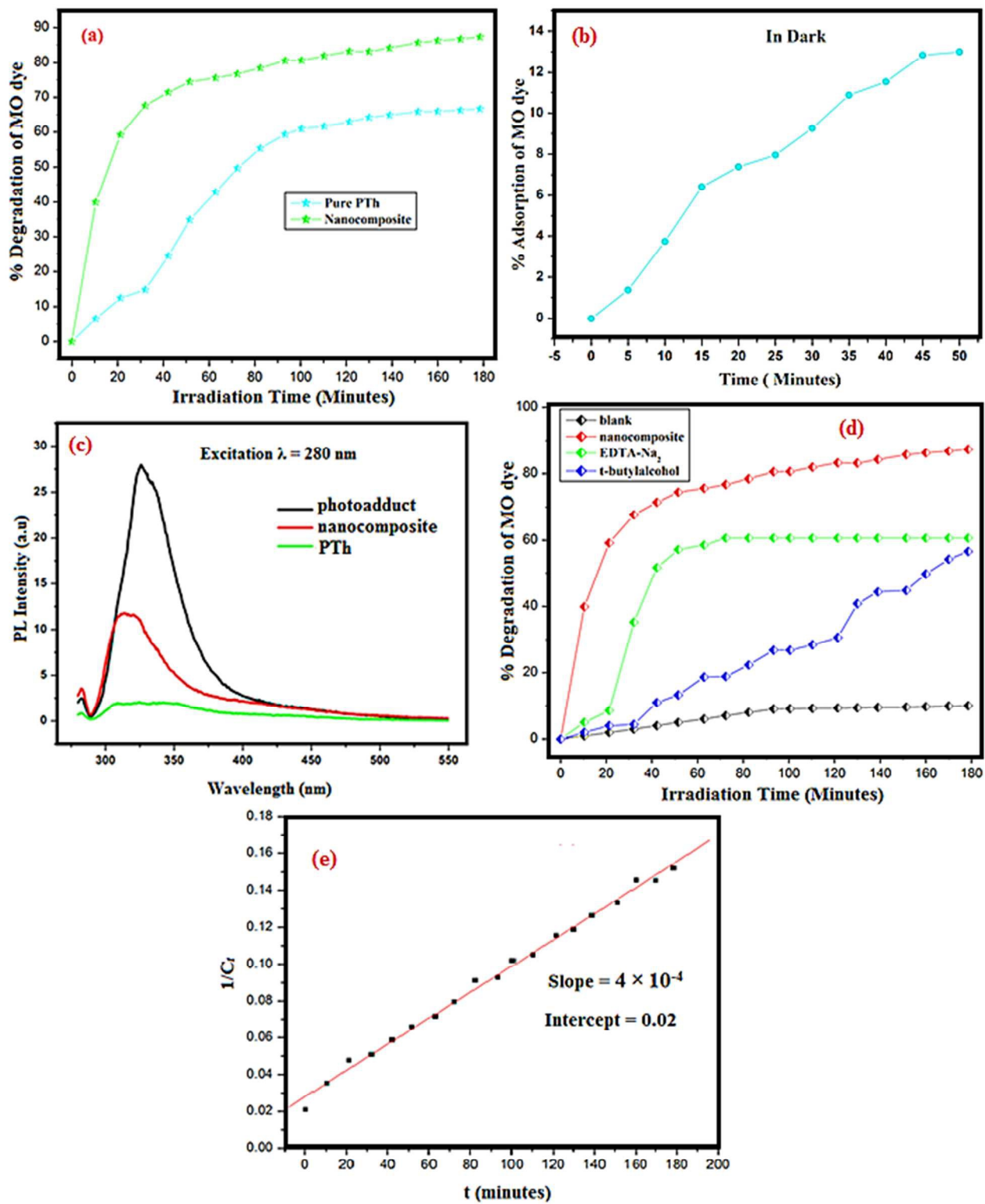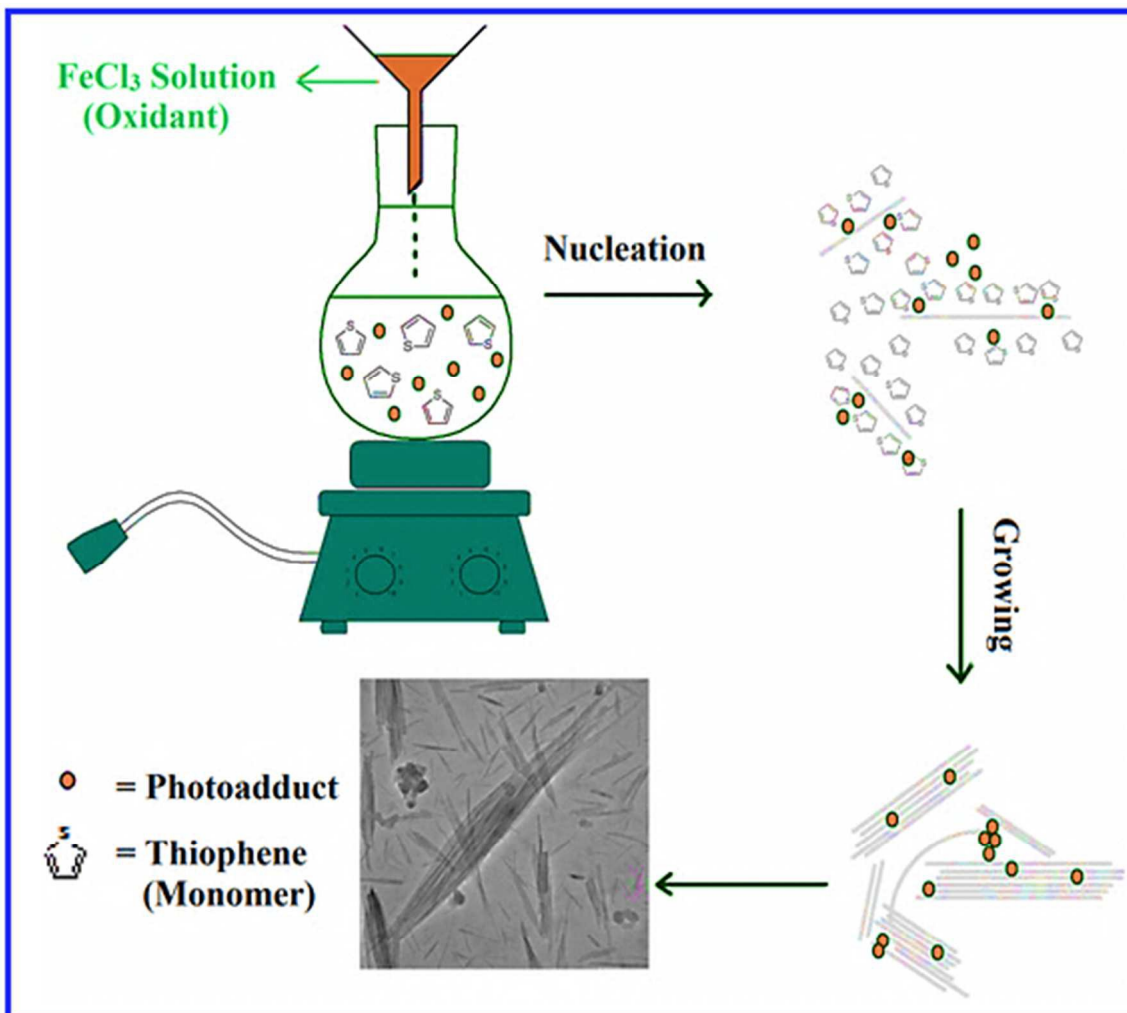
Scheme 1

Scheme 2
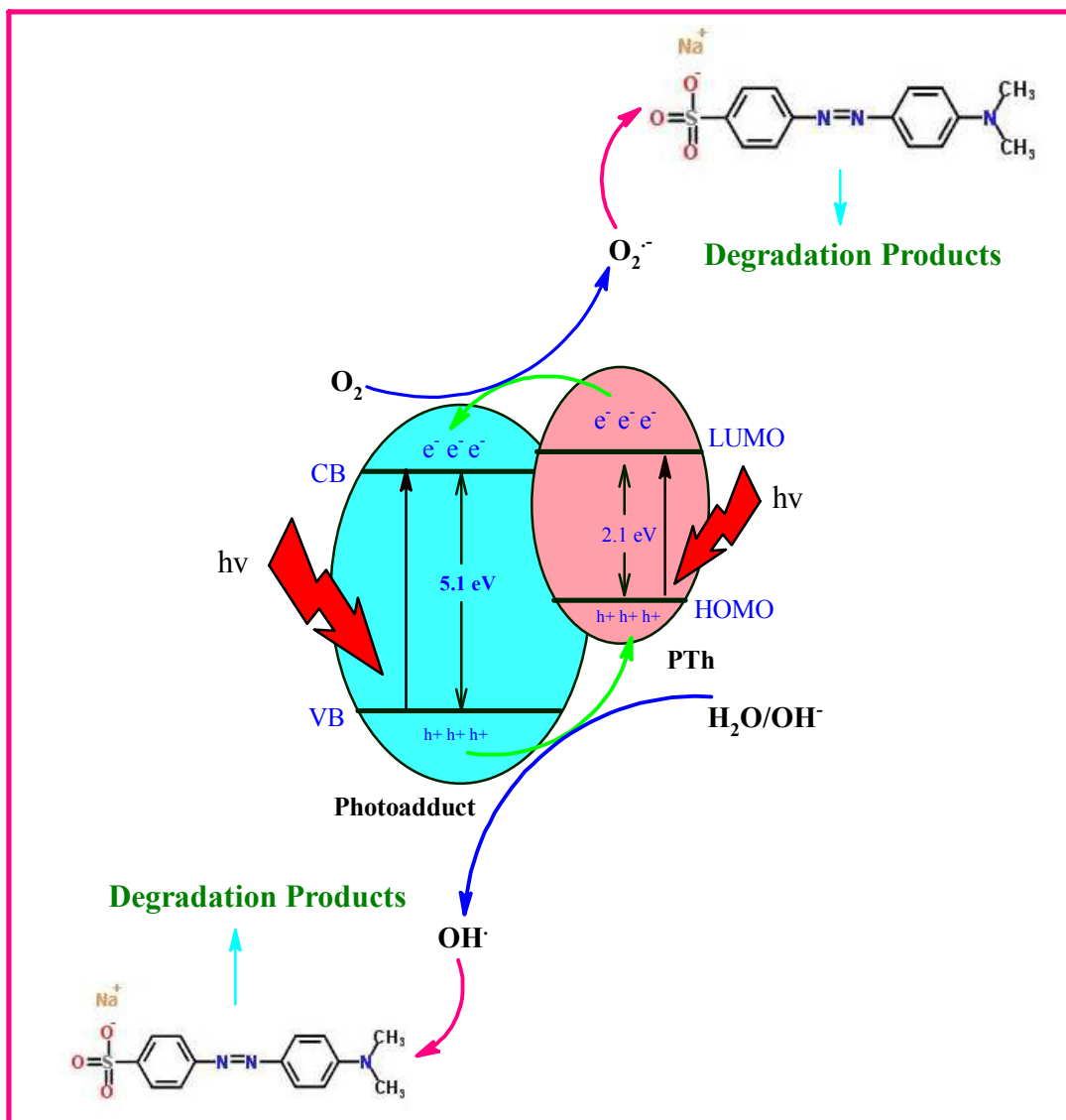
| System	Crystal Structure	Lattice parameters (Å)	Volume (Å³)	Size (nm)
Photoadduct	Orthorhombic	a= 13.88703, b= 14.77325, c=7.29169, α= 90, β=90 & γ=90	1495.93	25.5
Nanocomposite	Orthorhombic	a= 13.88325, b= 14.77267, c=7.29068, α= 90, β=90 & γ=90	1495.26	71.1

Table 1

9

| Materials	% Photodegradation of MO dye	References
PTh/[Fe(CN)$_3$(NO)(bpy)] 4H$_2$O	87	Present System
P25 Benchmark	40	[27], [28]
PTh/ZnO	70	[29]
PTh/Fe$_2$O$_3$/SiO$_2$	10	[30]
PTh/TiO$_2$	60	[31]
P3HT/ TiO$_2$	20	[32]

Table 2

Enhanced photocatalytic activity exhibited by PTh/[Fe(CN)$_3$(NO)(bpy)] 4H$_2$O nanocomposite fibers via a synergistic approach

Mohd. Hanief Najar[*], Kowsar Majid[*]
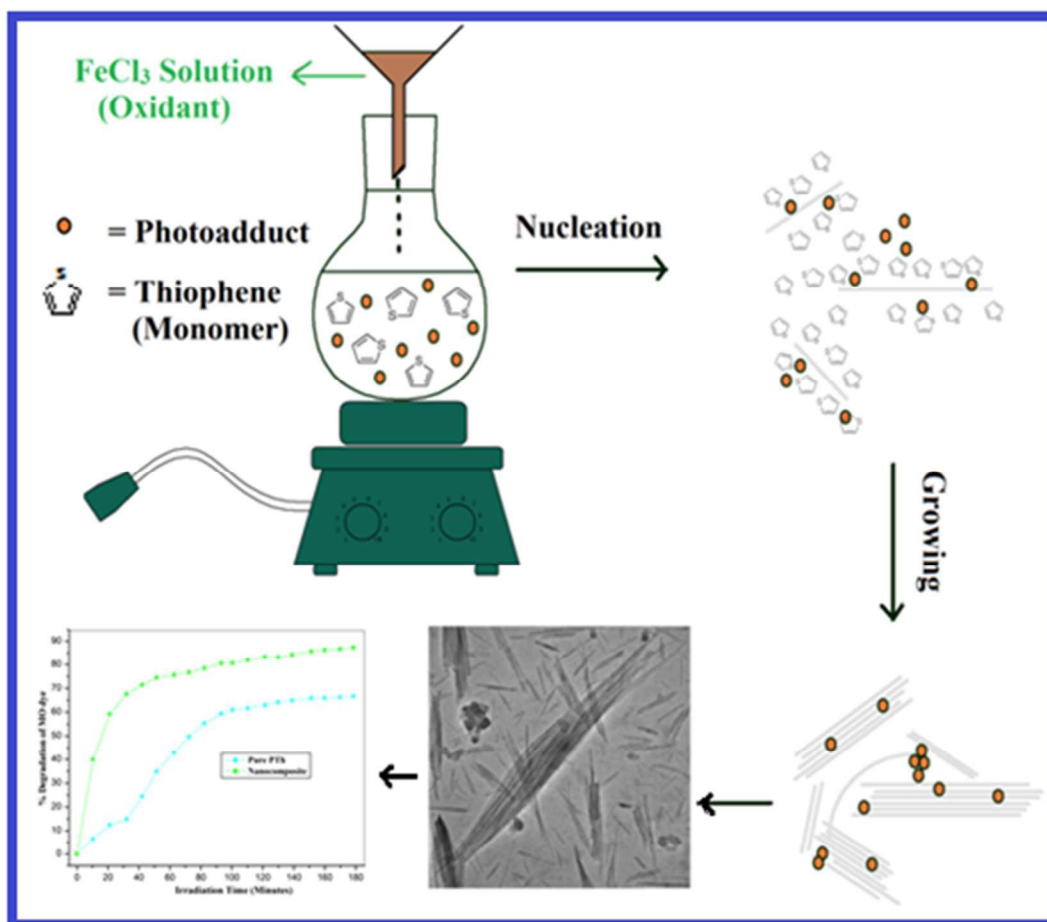
This shows the schematic representation of the synthesis of nanocomposite fibers with enhanced photocatalytic activity
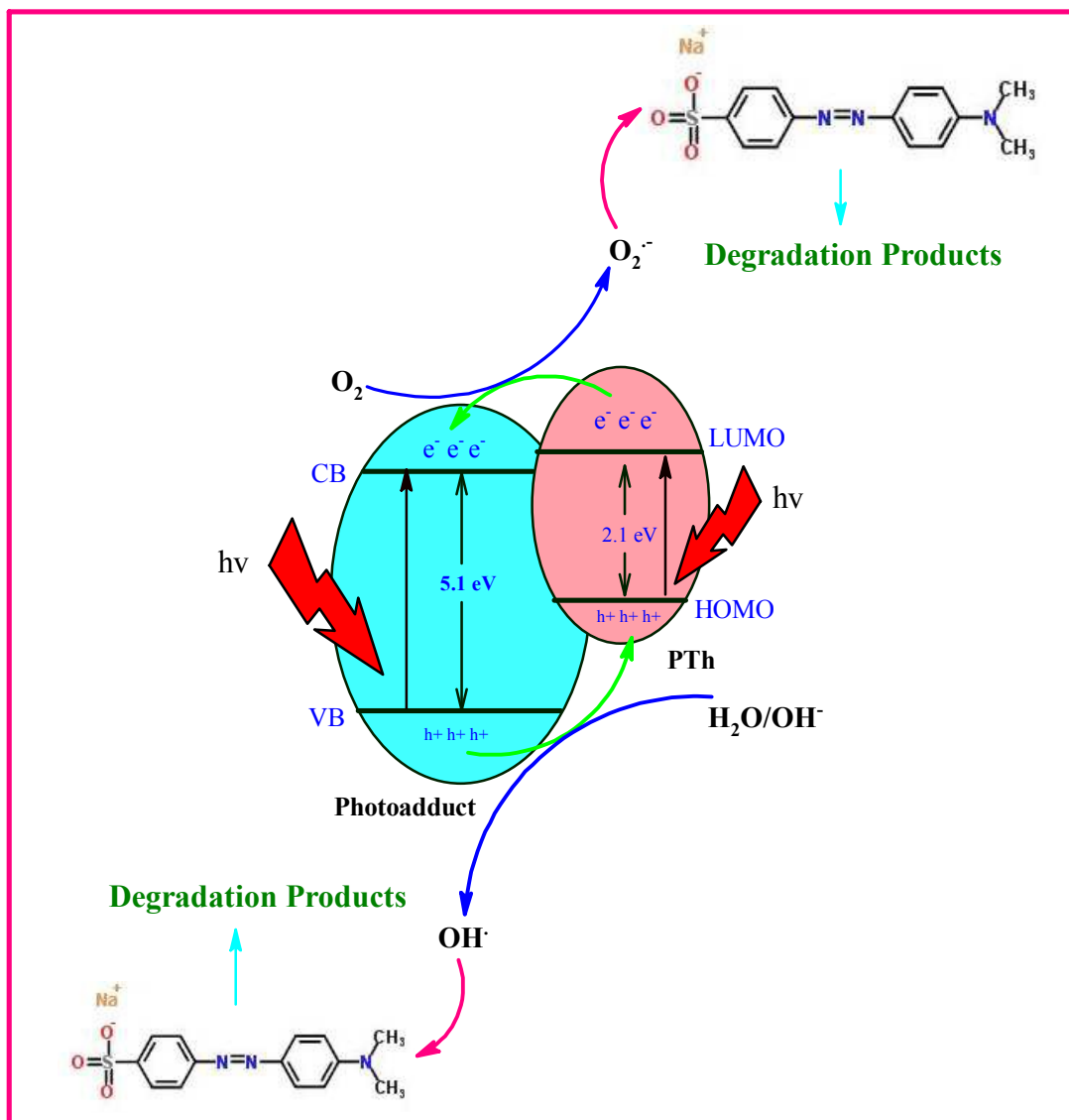
This reflects the proposed mechanism for the photo-degradation of MO dye using the synthesized photocatalyst (nanocomposite fibers)